DOI: 10.1021/ma9027883

Macromolecules
ARTICLE

Destabilization of Polyelectrolyte Multilayers Formed at Different Temperatures and Ion Concentrations

Matthias Cornelsen,[†] Christiane A. Helm,*[,‡] and Stephan Block[‡]

[†]*Antriebstechnik und Mechatronik, Universität Rostock, Justus-von-Liebig-Weg 6, D-18059 Rostock, Germany, and* [‡]*Institut für Physik, Ernst-Moritz-Arndt Universität, Felix-Hausdorff-Str. 6, D-17489 Greifswald, Germany*

Received December 18, 2009; Revised Manuscript Received March 24, 2010

ABSTRACT: Polyelectrolyte multilayers (PEMs) from poly(allylamine hydorchloride) (PAH) and sodium poly(styrenesulfonate) (PSS) are prepared at different conditions and investigated in air with X-ray reflectivity. Beyond a critical temperature the thickness per deposited polycation/polyanion bilayer and the surface roughness increase on heating the preparation solution. With increasing NaCl concentration that critical temperature decreases (40 °C at 1 M down to 15 °C at 3 M). Below the critical temperature the film thickness shows no dependence on the deposition temperature. Also, for ion concentrations up to 3 M, the surface roughness is constant (1−1.5 nm). However, for films prepared at 4 M the roughness increases on cooling, which is attributed to approaching the UCST at very high salt concentrations. AFM measurements in air show that the increased surface roughness is due to a random pattern of holes, whose separation is characterized by a single length scale, a behavior typical for spinodal decomposition. The length scale exceeds 100 nm and depends on the preparation conditions. Grains consisting of polyelectrolyte complexes with a size below 30 nm do not influence the surface roughness. It is suggested that the decomposition occurs during film drying since the film morphology in water shows no decomposition pattern, even when the film is cooled.

Introduction

Adsorbed polyelectrolytes are used not only in a multitude of technical applications (e.g., as wet and dry strength additives) but also in basic research in connection with material and the life sciences.[1−5] Because of their ionizable groups (incorporated within the monomeric units), polyelectrolytes can be used as flocculating or dispersing agent in industrial applications.[6,7]

Furthermore, by sequential adsorption of oppositely charged polyelectrolytes onto surfaces[3,8] it is possible to build polyelectrolyte multilayers (PEMs) onto solid substrates. The thickness of such PEMs can be influenced e.g. by the number of adsorption steps, the polyelectrolytes used, and the internal properties of the adsorption solution (e.g., ionic strength, temperature, and pH value). Hence, a control of the layer thickness with nanometer precision is possible[9] if the dependence of the PEM growth on the preparation conditions is known.

Therefore, theoretical efforts as well as experimental works have been done to understand the processes involved in sequential adsorption of polyelectrolyte layers. It is well established that a necessary condition for the formation of PEMs is the charge overcompensation (i.e., that the surface charge reverses its sign) after each adsorption step, in order to allow the oppositely charged polyelectrolyte to adsorb. Hence, the electrostatic interactions play an important role in the growth of PEMs.

The mechanism of the Debye screening shows that an increase in salt concentration reduces the magnitude of the electrostatic forces. Thus, by the addition of salt to the adsorption solution, it is possible to adjust the ratio between the electrostatic and nonelectrostatic forces. Therefore, theories that include electrostatic forces as the only attractive interaction between the polyelectrolytes and the substrate (or the PEM, respectively) show a pronounced adsorption−desorption transition if the salt concentration in the adsorption solution exceeds a critical value.[10,11]

However, this is in contrast to almost all experimental data published, which show in general an increase in polyelectrolyte surface coverage if the salt concentration is increased.[12−14] Therefore, we conclude that also (attractive) nonelectrostatic/secondary interactions play an important role in the growth of PEMs. In our opinion, these theories break down at high salt concentration because the electrostatic interactions become small compared to secondary interactions. This idea is underlined by recent works which show a pronounced increase in PEM thickness with rising adsorption temperature for weak and strong polyelectrolytes.[16−19]

Furthermore, the sequential adsorption leads to the formation of polyanion−polycation complexes, which can be imaged with atomic force microscopy (AFM).[20,21] Therefore, by imaging the surface morphology of PEM films, we address the question: if changes in the interaction between polyanions and polycations have an effect on the stability of PEM films, what can be determined from the conformation of the formed complexes?

Usually, the possibility of PEM formation is explored in a very straightforward way; either it works or it does not work. If it works, there are some characteristic parameters which can be influenced: the thickness increase per deposited polycation/polyanion bilayer and the interfacial roughness.[15] In this work we investigate complementary parameters: we measure the film/air roughness with X-ray reflectivity and monitor simultaneously the surface morphology with AFM. Thus, we intend to correlate surface morphology and roughness. Especially we want to explore the influence of the polycation/polyanion complexes described previously[20,21] on the roughness.

*To whom correspondence should be addressed.

 Published on Web 04/14/2010

On a more fundamental level, we are interested in the competitive interactions which influence the formation of polyelectrolyte multilayers. Very important is the electrostatic interaction. If its range and amplitude are reduced by an increase in ionic strength, secondary/nonelectrostatic interactions gain importance, which may affect polyelectrolyte adsorption. Indeed, at high ion concentrations and increased preparation temperature the thickness per deposited bilayer and also the interfacial roughness are increased.[17−19] These features are attributed to the hydrophobic interaction, whose signature is its temperature dependence. To investigate the influence of the various inter- and intermolecular forces on the film/air interface, the preparation parameters ionic strength and preparation temperature are varied systematically.

Materials and Methods

All solutions are created with ultrapure water using a Milli-Q device (Millipore, Billerica, MA). Sodium chloride (NaCl, p.a. grade) was obtained from Merck (Darmstadt, Germany). Sodium poly(styrenesulfonate) (Na-PSS) with an average weight of $M_w = 70$ kDa and PDI < 1.1 was purchased from Polymer Standard Service (Mainz, Germany), whereas poly(ethylenimine) (PEI) and poly(allyamine hydrochloride) (PAH, $M_w = 70$ kDa) were obtained from Sigma-Aldrich (Steinheim, Germany). All chemicals are used without further purification.

Deposition Solutions. To study the influence of salt concentration I and temperature T on the multilayer growth, several polyelectrolyte deposition solutions are prepared: each solution is created by dissolving 3 mM of the respective polyelectrolyte (with respect to the monomer concentration) in Milli-Q water, and afterward the salt concentration is set to a value between 0.15 and 4 M by dissolving the appropriate amount of NaCl within the polyelectrolyte solution.

Surface and Multilayer Preparation. The PEM films are prepared by sequential adsorption of polyelectrolyte layers[3,8] on silicon wafers (Wacker Siltronic AG, Burghausen, Germany). The wafer are cleaned according to the RCA standard and freshly used. Before deposition all solutions (to be used) are heated to the designated deposition temperature using a thermostat (Thermo Haake, Karlsruhe, Germany). The only exception to this rule is the PEI solution, which is not heated above 25 °C.

After reaching equilibrium temperature, the multilayers are created by immersing the cleaned silicon wafers in the polyelectrolyte deposition solutions of given salt concentration as follows: the first layer of each PEM is a PEI precursor layer, followed by a certain amount n of PSS/PAH bilayers. This leads to the PEM architecture PEI/[PSS/PAH]$_n$ and hence to a $n + 0.5$ bilayer sample.

Between each deposition step unbound polyelectrolytes are removed by washing the silicon wafer three times in pure Milli-Q water for 1 min. For each washing step fresh Milli-Q water is used, which has the same temperature as the deposition solution.

The whole deposition process is automated by using a programmable dipping robot purchased from Riegler & Kirstein (Berlin, Germany). However, during deposition the operator has to make sure that the sample is not dried during the transfer between the solutions (this is a noticeable problem at deposition temperatures exceeding 40 °C) as drying of the sample might lead to crystallization/incorporation of salt on/within the PEM film. This is achieved by keeping the surface wet using a washing bottle containing Milli-Q water of the appropriate temperature.

X-ray Reflectometry (XRR). The PEM films are investigated with a Seifert XRD 3003 TT diffractometer (Seifert, Germany) in X-ray reflection setup using Cu Kα radiation ($\lambda = 1.54$ Å). This results in X-ray reflection curves (cf. Figure 1), which provide accurate information about the electron density variation perpendicular to the surface.[22] However, during conventional XRR measurements the phase information is lost, and hence, the analysis of the XRR data is based on finding a suitable electron density profile of the PEM film.

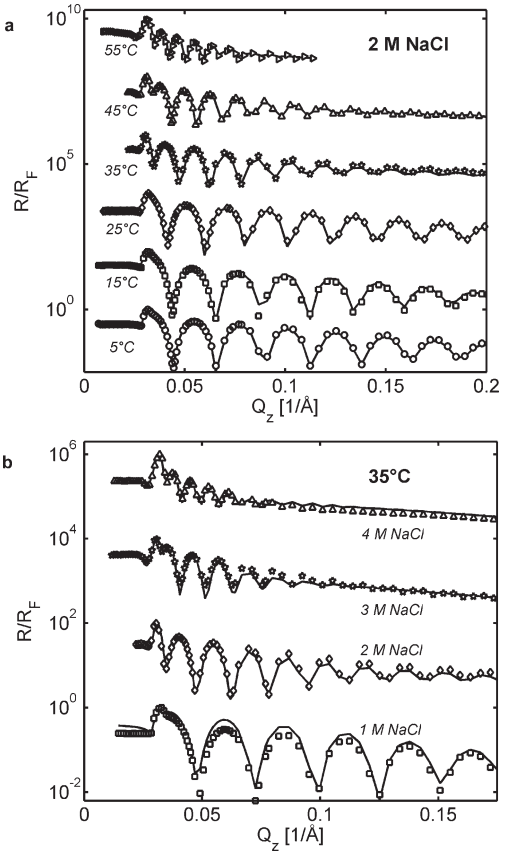

Figure 1. Representative Fresnel-normalized X-ray reflection curves obtained from 6.5 bilayer samples prepared as indicated (a) at constant ionic strength $I = 2$ M NaCl and different deposition temperatures or (b) at constant deposition temperature $T = 35$ °C and different salt concentrations. For clarity, the curves are shifted vertically relative to each other. The original data are given by the symbols and the fit to a one-slab model by the solid lines. Additional X-ray reflection curves can be found in the Supporting Information.

Therefor, the PEM film is modeled by a homogeneous slab (exhibiting a slab length = the total PEM film thickness d_{PEM}, a film−air roughness σ, and an electron density of the PEM film n_{PEM}), which is situated onto a silicon substrate with a certain roughness σ_{Sub} and electron density n_{Sub}. Using the Paratt algorithm,[23] it is possible to calculate the exact X-ray reflection curve for each PEM model. Hence, the model parameters for each sample can be obtained by performing a root-mean-square (rms) fit of the calculated reflection curves to the measured data.[24] Afterward, for each PEM the (average) bilayer thickness d_{BL} is calculated by dividing the film thickness by the total bilayer count, i.e., $d_{BL} = d_{PEM}/(n + 0.5)$.

Surface Morphology. AFM imaging is performed in air and liquid using a Multimode atomic force microscope (purchased from Veeco/Digital Instruments, Santa Barbara, CA), which is equipped with a Nanoscope IIIa controller. The AFM piezo scanner was calibrated using calibration gratings TGZ01 (rectangular 26 nm SiO_2 steps on silicon wafer; manufacturer: MicroMash, Tallin, Estonia) and PG (chessboard-like pattern on silicon, 100 nm depth and 1 μm pitch; manufacturer: Digital Instruments, Santa Barbara, CA).

The images are recorded with Tapping Mode in air using standard tapping mode cantilevers (OMCL-AC160TS, Olympus, Hamburg, Germany) and in liquid using D-NPS cantilever from Veeco/Digital Instruments (Santa Barbara, CA). Before usage the cantilevers are tested with a Nioprobe self-imaging

sample (Aurora Nanodevices, Nanaimo Canada), and only cantilevers with tip radius <10 nm (air) and <25 nm (liquid) are used for imaging. Images are obtained from at least five different positions of the sample and in five different resolutions ranging between 500 nm and 10 μm scan size.

AFM Image Processing. Images obtained with the AFM are stored in raw data format, i.e., in absence of any automated filtering or image processing by the AFM software. Afterward, the images are processed using the Nanoscope 5 software (which is delivered with our commercial DI Multimode AFM) as follows: For larger images (scan area $>1 \times 1$ μm^2) the spherical distortion introduced by the piezo scanner is removed by fitting a spherical plane (of second order) to the data and by subtracting the fitted spherical plane from the data. For smaller images this correction is skipped, as no distortion is noticeable.

Determination of Coarse Structure Wavelength. Using the Nanoscope 5 software, a two-dimensional fast Fourier transformation (2D FFT) of the images is calculated, leading to a 2D power spectrum $S_2(\lambda_x^{-1},\lambda_y^{-1})$ of the entire image over spatial wavelengths λ_x and λ_y. In case of images that exhibit a coarse structure, the 2D power spectrum shows radial symmetry with a preferred spatial wavelength (see Supporting Information). Hence, the directional information on the 2D power spectrum is removed by radially averaging: for a given radial wavelength λ, the isotropic 2D power spectral density (i2D-PSD) is defined by

$$\mathrm{PSD}(\lambda) = \frac{\lambda}{2\pi}\int_0^{2\pi} S_2\left(\frac{\cos\phi}{\lambda},\frac{\sin\phi}{\lambda}\right)\mathrm{d}\phi$$

and exported into an ACSII file. For a given preparation condition all i2D-PSDs are imported in MatLab (MathWorks, Natick, MA) and averaged (over the radial wavelength λ) in order to reduce the noise within the i2D-PSD.

Determination of the Fine Structure Wavelength. In all images globular objects with a size of several 10 nm are visible. To quantify the length scale of this fine structure, we employ the following approach: A home-written script[25] in MatLab scans the AFM images for local maxima, whose positions are assumed to be the tops of the globular objects. The (such-like-determined) lateral positions of the tops are stored and marked by a circle in the images (cf. Supporting Information). Using these data, we are able to calculate for each object the lateral distance to all other objects and to average the lateral distance of each object to its six next neighbors (suggesting a hexagonal ordering of the objects as a first approximation). A histogram of these average distances shows a pronounced peak (cf. Supporting Information), indicating that there is a preferred average distance between the objects. Hence, the length scale of the fine structure is set to the maximum in the histogram. Please note that the usage of four and eight next neighbors (instead of six) gives very similar results for this length scale.

Results and Discussion

Figure 1 shows representative, Fresnel-normalized X-ray reflection curves obtained from 6.5 bilayer samples (prepared as indicated). Further X-ray reflection curves can be found in the Supporting Information. The figures show that an increase in salt concentration I and temperature T of the deposition solutions decreases the distance between minima of the curve, which indicates an increase in film thickness d_{PEM} of the PEM. Furthermore, the damping of the Kiessig oscillations increases with increasing salt concentration I and temperature T and shows an increase in air−film roughness σ.

Both film properties are quantified using a one-slab model, which is fitted to the reflection data according to the Materials and Methods section. In Figure 1 these fits are given by solid lines and give a good description of the XRR data. The parameter

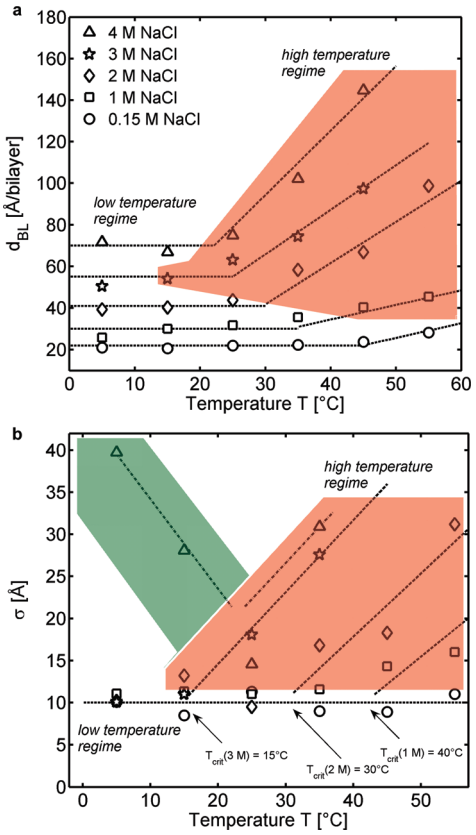

Figure 2. Parameter plots for (a) the average bilayer thickness $d_{BL} = d_{PEM}/(n+0.5)$ and (b) the film−air roughness σ as obtained by fitting a one-slab model to the reflectivity data of the PEM samples (prepared as indicated). The data can be grouped into two regimes: in low temperature regime the parameters show little or no dependence on T, whereas in high temperature regime (red shaded area or roughness σ exceeding 10 Å) there is a strong increase with raising T. The critical temperature T_{crit} between both regimes decreases with increasing salt concentration I. The only data that are inconsistent with this observation are the roughness data for $I = 4$ M NaCl and will be discussed separately (green shaded area).

plots for the bilayer thickness d_{BL} and the air−film roughness σ can be found in Figure 2a,b.

If we neglect for a second the roughness data for samples prepared at $I = 4$ M NaCl (which will be discussed separately at the end), each parameter set of Figure 2 falls into one of two different regimes: at low temperatures, there is no or very little effect of the deposition temperature on bilayer thickness or roughness, whereas at higher temperatures both quantities are strongly increased by a raise in deposition temperature T. Therefore, we will denote these regimes as low and high temperature regime, respectively.

Furthermore, the parameter plots show that in the low temperature regime it is possible to increase the bilayer thickness d_{BL} by adding salt to the deposition solution (an increase from 0.15 to 4 M NaCl increases the bilayer thickness by at least a factor of 3.5), whereas the film−air roughness σ remains constant at ~10 Å, which is close to the values that are often reported for PAH/PSS bilayer roughness in the literature.[17] This is an interesting property because σ seems to be independent of the total film thickness or number of deposited bilayers.

In the high temperature regime (red shaded area in Figure 2) both quantities d_{BL} and σ rise with increasing temperature. Hence, the critical temperature T_{crit} from low to high temperature regimes can be defined by the temperature where the roughness starts to deviate from 10 Å. This gives $T_{crit} = 40$, 30, and 15 °C for $I = 1$, 2, and 3 M NaCl, respectively. A comparison with the

bilayer thickness in Figure 2a shows that T_{crit} (defined by an increase in σ) gives a reasonable measure for the critical temperature: for $T > T_{crit}$ the bilayer thickness d_{BL} exhibits a strong dependence on the deposition temperature T, whereas for $T < T_{crit}$ it does not.

We assume that both regimes describe two different kinds of bilayer growth: The roughness increases only if the critical temperature T_{crit} is exceeded for the given salt concentration and hence if the bilayer thickness d_{BL} shows a strong temperature effect. Therefore, it is reasonable to say that the "additional" bilayer growth in high temperature regime is always accompanied by a roughening of the PEM. However, the same increase in bilayer thickness can also be obtained by an increase of the salt concentration I, which is not accompanied by an increase in roughness in the low temperature regime. For example, an increase in temperature from 5 to 55 °C at I = 1 M NaCl almost doubles the bilayer thickness and roughness. But the same increase in bilayer thickness is also obtained by rising the salt concentration from I = 1 M NaCl to 3 M NaCl at T = 5 °C, whereas the roughness remains constant under these conditions. This shows that an increase in bilayer thickness is not automatically accompanied by an increase in film−air roughness; it depends strongly on the growth regime of the PEM.

Another way to inspect the bilayer thickness is to plot d_{BL} versus the square root of the salt concentration I (cf. Figure 3). This approach is motivated by the work of Hesselink, who predicted for strong polyelectrolytes a linear relationship between the surface coverage (i.e., adsorbed polyelectrolyte mass per unit area) and $\sqrt{I}$.[26] This prediction is supported by experimental measurements (performed on single polyelectrolyte layers[27] and multilayers[28]) and numerical simulations using self-consistent-field (SCF) methods.[29,30] Interestingly, the SCF simulations show that a certain salt concentration has to be exceeded to establish the linear relationship and that the surface coverage is almost independent of I below this salt concentration. Furthermore, these simulations also indicate that the $\sqrt{I}$ law even holds at salt concentrations exceeding 1 M. This is counterintuitive as (under these conditions) the Debye length κ^{-1} (i.e., the length scale of the electrostatic force and given by $\kappa^{-1} = 0.304\ \text{nm}/\sqrt{I}$ for solutions of monovalent salts at 25 °C, where I is measured in mol/L) falls below the length scale of single water molecules, and hence, a failure of these mean-field approaches becomes likely.[31]

A similar relationship can be found in our data (cf. Figure 3). However, the data cannot be completely explained by a simple square root dependence of d_{BL} on I, as reported in the literature.[27,28] Again, the bilayer thickness can be grouped into two different regimes: for I < 1 M NaCl (low salt regime) there is a slight effect of the temperature on the bilayer thickness (which was already reported by Gopinadhan et al.[19]), whereas for I > 1 M (high salt regime) the bilayer thickness shows a strong temperature effect for T > 25 °C.

Surface Morphology. However, one has to ask which mechanism causes the increase in film−air roughness. One suitable method is the investigation of the film−air interface by atomic force microscopy (AFM), which has the advantage that the information obtained by X-ray reflectometry (PEM film thickness and film−air roughness) can be supplemented by lateral (e.g., film morphology) as well as vertical (cf. rms roughness) film properties.

A representative set of AFM images is given in Figure 4, which presents the morphology of PEMs deposited at 2 M NaCl for temperatures as indicated in the images. AFM images obtained at the remaining salt concentrations can be found in the Supporting Information. Obviously for T < 35 °C the film appears homogeneous and exhibits only a fine structure (cf. Figure 8 for a higher resolved image). For $T \geq$ 35 °C (> T_{crit} for 2 M NaCl) an additional lateral structure is revealed by AFM, whereas the length scale of this structure is much larger than the fine structure. This structure consists of holes and rifts whose depth increases with temperature (cf. Figure 4c−e) and will be called coarse structure in the following.

The same behavior is found for the other salt concentrations: i.e., a rather homogeneous film (showing only the fine

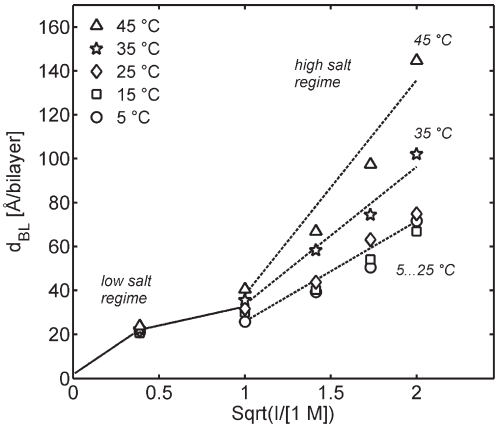

Figure 3. Bilayer thickness d_{BL} plotted versus the square root of the salt concentration I in the deposition solutions. Again, the data can be divided into a low and a high salt regime: For I < 1 M NaCl (low salt regime) the bilayer thickness is independent of T within experimental accuracy. However, for $I \geq$ 1 M NaCl a temperature effect on d_{BL} becomes noticeable for deposition temperatures exceeding 25 °C. Furthermore, the plot shows that in the high salt regime d_{BL} depends linearly on the square root of I. This is established theoretically and experimentally for polyelectrolyte monolayers but seems to be valid also for PEMs.

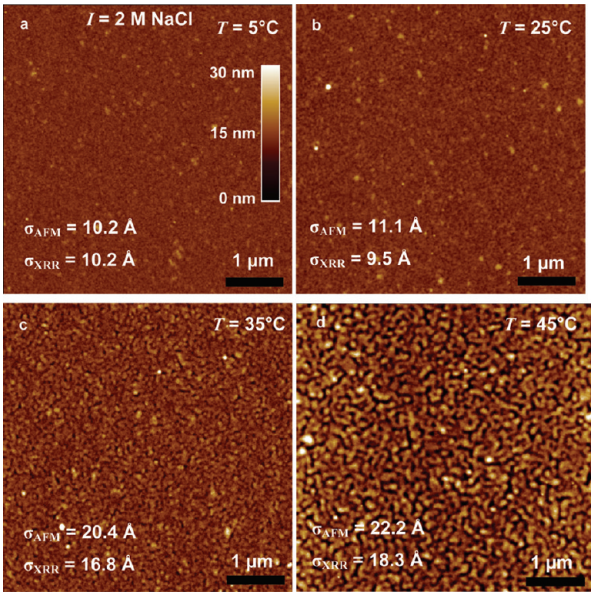

Figure 4. Surface morphology of 6.5-bilayer PEM prepared at constant I = 2 M NaCl and at deposition temperatures as indicated. Below the critical temperature T_{crit}(2 M NaCl) = 30 °C the surface of the PEM shows only few inhomogeneities, and these films exhibit a surface roughness around 10 Å. Higher resolved images show (e.g., Figure 8) that the surface morphology is best described by a closed packing of globular objects with a length scale < 100 nm (fine structure). However, after exceeding T_{crit}(2 M NaCl) the film shows the beginning of spinodal decomposition and corrugations appear on a large length scale (coarse structure). The comparison of the surface roughnesses (obtained by AFM or XRR) gives a good agreement between these complementary techniques and shows that the increase in surface roughness is caused by the coarse structure.

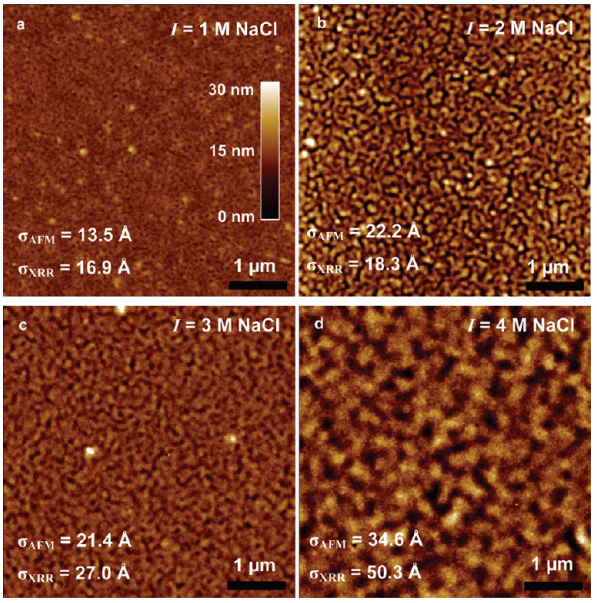

Figure 5. Surface morphology of 6.5-bilayer PEM prepared at constant deposition temperature $T = 45$ °C and at deposition salt concentration I as indicated (Figure 5b is the same as Figure 4d). Obviously, the length scale of the coarse structure increases with increasing I. To quantify this behavior, isotropic two-dimensional power spectral densities (i2D-PSDs) of the AFM images are calculated (cf. Figure 6).

structure) for $T < T_{crit}$ and a lateral structuring (coarse structure) for $T > T_{crit}$. The length scale of the coarse structure slightly increases with rising deposition temperature T. Furthermore, we found good agreement between the film roughness as determined by XRR and AFM (cf. Figure 4).

This observation gives more substance to the idea that the layer built up differs in the low and high temperature regimes: the AFM shows that the increase in roughness (which is a result of the "additional" bilayer growth in the high temperature regime) is caused by an additional coarse structure of the film−air interface of the PEM and hence that both regimes lead to different surface structures, which can be distinguished using the AFM.

To understand the different regimes, we will investigate now the dependence of the coarse and fine structure on I and T.

Film-Surface Structure: Coarse Structure Due to Spinodal Decomposition. In the previous section we showed that the surface structure of the multilayer exhibits a coarse structure, if the layers are deposited above T_{crit}, and that this coarse structure leads to an increase in film−air roughness σ. The latter is also observed with XRR.

Figure 5 shows AFM images of PEM films prepared at 45 °C and at salt concentrations as indicated. We have chosen this temperature as all these multilayers show an increased roughness and hence a coarse lateral structure. Obviously, the length scale of the coarse structure is on the order of serveral 100 nm (which is an increase of 1 order with respect to the fine structure) and increases with increasing salt concentration.

However, the surface morphology of the coarse structure (cf. Figure 5) is very similar to surface structures, which are observed in films that exhibit spinodal decomposition.[32,33] Apparently, the separation of the ridges is rather constant. This observation will be quantified below. In general, decomposition of a mixture of two or more components is often observed, if the phase diagram of the mixture exhibits a miscibility gap. Within this gap the (resulting) free energy of the separated components has a smaller value compared to the case of homogeneously mixing components, and hence, decomposition of the mixture is thermodynamically preferred if the composition of the mixture changes in such way that the miscibility gap is entered.

Usually, two different decomposition schemes can be observed: nucleation of the components into two different homogeneous phases and spinodal decomposition. Both schemes differ in several properties, which often allows an identification of the acting scheme. For example, nucleation leads to a decomposition which is localized at discrete nucleation sites, whose position and size are usually randomly distributed. Often, a critical size of the nucleus has to be exceeded to allow a spontaneous growth and hence a self-contained decomposition of the mixture.

By contrast, a spontaneous decomposition of the mixture will occur if the second derivative of the free energy G (with respect to the mole fraction) is negative. This kind of decomposition is called spinodal, and the domain within the miscibility gap fulfilling the requirement $G'' < 0$ is denoted as spinodal region.

Theoretical considerations show that the decomposition is caused by a spontaneous amplification of thermally excited concentration fluctuations, which are distributed over the whole mixture. Interestingly, using the model of Cahn and Hilliard,[34] it can be shown that only those concentration fluctuations will be amplified whose spatial wavelength exceeds a critical wavelength λ_{crit} and that the fastest growing fluctuations exhibit the wavelength $\lambda_{SD} = 2^{1/2}\lambda_{crit}$.[35] Hence (in contrast to nucleation), spinodal decomposition leads to spatially periodic structures whose length scale is given by λ_{SD} and which are very similar to those depicted in Figure 5.[33]

To quantify this length scale, we calculate the isotropic two-dimensional power spectral densities (i2D-PSDs, cf. Materials and Methods section), and the results for the images of Figure 5 are given in Figure 6c. The i2D-PSDs show an pronounced peak which can be related to the average distance between adjacent holes of the coarse structure. Obviously, the peak shifts with increasing salt concentration to higher wavelengths (cf. Figure 6d), as the images in Figure 5 suggest. The effect of the deposition temperature T on the length scale of the coarse structure is much smaller (cf. Figure 6b).

Origin of the Spinodal Decomposition. At the moment, spinodal decomposition of the PEM appears to be thermally activated as a critical deposition temperature T_{crit} (which depends on I) has to be exceeded to start this process. Hence, the decomposition seems to be started by a temperature quench that occurs during cooling of the PEM (i.e., the decrease in PEM temperature from the deposition to the room temperature). However, in the following we will show that this is not an appropriate description and that the destabilization of PEMs due to spinodal decomposition is caused by a change in forces acting during the deposition of the PEM.

This can already be inferred from Figure 7, which shows the surface morphology of PEMs prepared at $I = 4$ M NaCl. Obviously, decomposition of the PEMs occurs for temperatures ≥35 °C and, surprisingly, also for temperatures below 15 °C. This is completely in contradiction to the assumption that the decomposition is a purely thermally activated process. Furthermore, this observation also explains why the roughness data for $I = 4$ M NaCl deviate from the qualitative behavior of the other samples: PEMs prepared at 4 M NaCl show two critical temperatures (an upper and

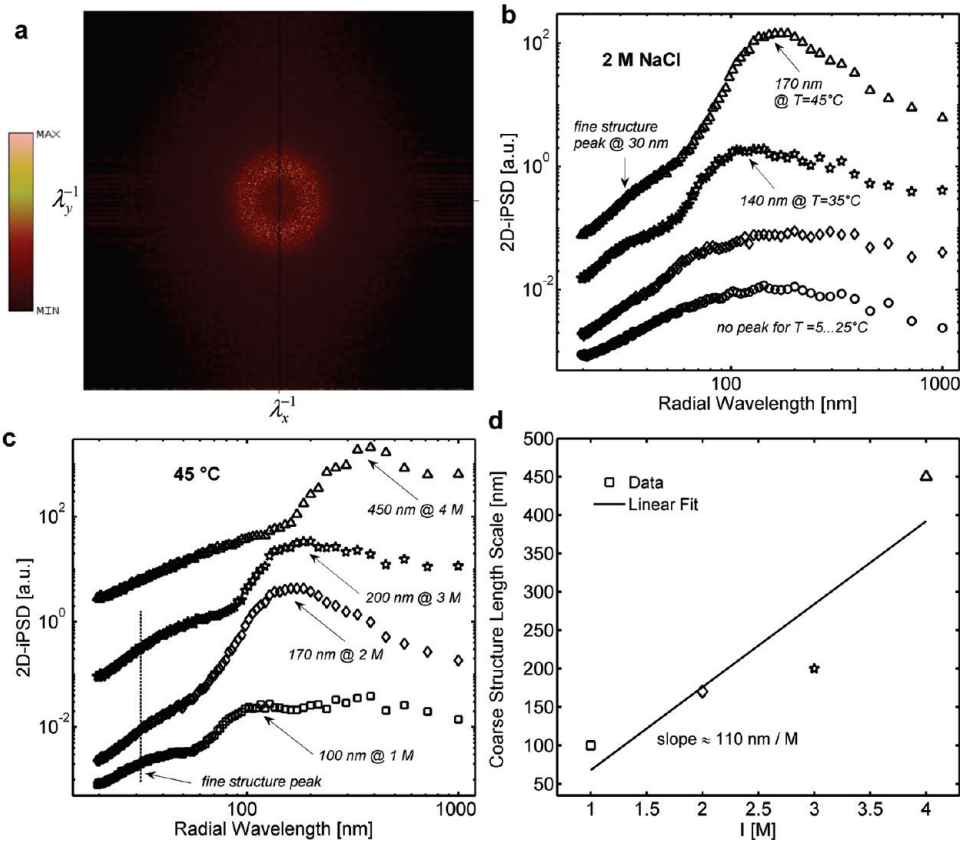

Figure 6. (a) FFT power spectrum of Figure 5b and isotropic two-dimensional power spectral densities (i2D-PSDs) of PEM films prepared at (b) constant $I = 2$ M NaCl and T as indicated or at (c) constant $T = 45$ °C and I as indicated. For constant I the transition from low to high temperature regime is also visible in the i2D-PSDs due to the formation of a pronounced peak < 200 nm. This peak can be attributed to the average distance between neighboring corrugations (cf. Figure 4c,d) and measures the length scale of the coarse structure. However, its increase with rising T is much smaller than the increase with rising I. Therefore, only the dependence on I is plotted in (d).

lower one), whereas all other samples exhibit (at the most) only one T_{crit}.

However, the existence of an upper and lower critical temperature suggests[30] that the occurrence of decomposition might be related to a change in solvent quality (with respect to I and T) of the adsorption solution. To investigate this idea, we have to take a closer look at the fine structure of the PEMs.

Film Morphology: Fine Structure. Figure 8 shows the fine structure of a PEM (prepared at $I = 0.15$ M NaCl and $T = 55$ °C), which consists of globular objects, whose size depends on the preparation conditions. To quantify the length scale of this fine structure, we employed an algorithm (cf. Materials and Methods section) that detects the center position of the complexes in the AFM images (cf. red circles in Figure 8). Afterward, the average lateral distance to their next neighbors is calculated, which is taken to be the length scale of the fine structure.

The dependence of this length scale on deposition temperature T and salt concentration I is given in Figure 9. Interestingly, this parameter behaves diametrically opposite to d_{BL} or σ: at low salt concentrations there is a large temperature effect on the fine structure length scale, whereas for $I \geq 3$ M the length scale becomes independent of the temperature and remains constant at ~29 nm (which seems to be an upper boundary for this system; cf. Figure 9). Furthermore, at low salt concentrations the length scale of the fine structure increases with increasing temperature until it reaches 29 nm at a certain temperature T_{Trans}, whereas T_{Trans} increases for decreasing I.

In refs 20 and 21 these complexes are attributed to aggregates of polyelectrolyte chains. Therefore, we calculate an average polyelectrolyte amount within one complex as follows: First, we assumed that the complexes can be approximated by spheres and that the fine structure is created by a closed packing of these spheres. In this view the diameter of the spheres would be the length scale of the fine structure. From the contour length of both polyelectrolytes and the requirement of charge neutrality we further assume that one PAH/PSS aggregate is composed of one PAH chain, which aggregates with 2.5 PSS chains. Using the molecular volume of one PAH or one PSS chain (80 or 60 nm^3, respectively), the volume of one PAH/PSS aggregate is 230 nm^3. Hence, from the diameters of Figure 9 one can calculate the volume of one complex and hence the amount of PAH/PSS aggregates within one complex. We find that there are between 8 (at a diameter of 15 nm) and 60 PAH/PSS aggregates (at a diameter of 30 nm) forming one complex.

Complex Growth and Solvent Quality. We will now relate the growth of the polyelectrolyte complexes with the forces acting between the monomers and connect these considerations to the solvent quality. The conformation of the polyelectrolyte within solution is ruled by a delicate balance between attractive and repulsive forces that are acting between the charged monomers. Usually (i.e., in noncollapsed state of the polyelectrolyte chain) there is an electrostatic repulsion between the monomers, which leads to a stretching of the chain and increases the end-to-end distance of the chain. However, a stretching reduces the conformational freedom of the monomers and creates a rising entropic force, which opposes this stretching. The equilibrium

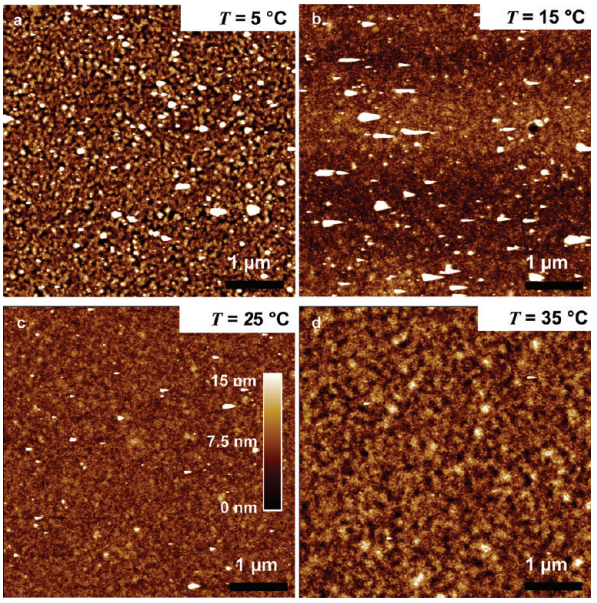

Figure 7. Surface morphology of 6.5-bilayer PEM prepared at $I = 4$ M NaCl and T as indicated (cf. Figure 5d for $T = 45$ °C). Interestingly, spinodal decomposition of the PEM occurs for $T \leq 15$ °C and $T \geq 35$ °C. This supports the idea that by approaching the upper and lower critical solution temperatures (UCST and LCST, respectively) of the polyelectrolytes the worsening of the solvent quality leads to a different deposition mechanism for the PEMs, which is dominated by none-lectrostatic/secondary interactions. This makes the PEM less stable and leads to spinodal decomposition upon drying of the PEM.

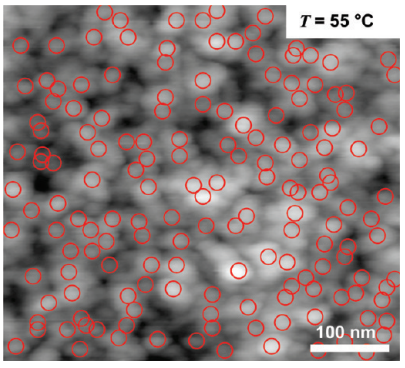

Figure 8. Fine structure of a 6.5-bilayer PEM prepared at $I = 0.15$ M NaCl and $T = 55$ °C. The surface exhibits closed packed globular objects, which are attributed to be PAH−PSS complexes. To estimate the size of these complexes, a home-written algorithm detects the top of each complex and marks it with a red circle.[25] In the next step, for each complex top the average distance to the tops of its neighbors is calculated. A histogram over all average distances shows a pronounced peak (see Supporting Information) which is taken to be the length scale of the fine structure (cf. Figure 9).

conformation is given by an end-to-end distance, where both forces cancel each other.[30]

However, this balance can easily affected by changes in I and T:

(i) An increase in I leads to a screening of the charges and reduces the electrostatic repulsion. With rising I the balance is shifted toward the attractive forces, and the polyelectrolyte starts to collapse. For a certain salt concentration the electrostatic repulsion equals the attractive interactions, and the net interaction on the monomers vanishes (theta condition). Hence, the polyelectrolyte can be approximated by an ideal chain of noninteracting monomers (Gaussian coil).

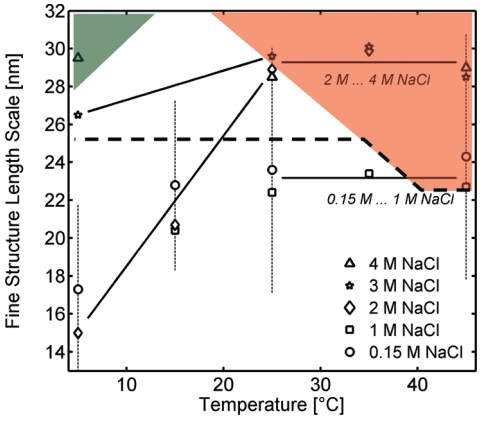

Figure 9. Length scale of the fine structure shows a diametrically opposite behavior to the bilayer thickness and the surface roughness: for small deposition salt concentrations there is a strong influence of the deposition temperature on this length scale, whereas at high salt concentrations the length scale is independent of the deposition temperature. The dashed line separates the values of I and T, which are expected to give good solvent conditions from the values that are expected to worsen the solvent quality. Furthermore, the shaded areas gives the preparation conditions, which lead to a coarse structure (spinodal decomposition) of the PEM. Interestingly, decomposition conditions coincide with bad solvent conditions. The vertical dashed lines give the standard deviation of the fine structure length scale for $I = 0.15$ M NaCl and shows that the observed shift is significant.

(ii) Furthermore, exceeding the temperature above a certain value introduces an additional attractive interaction to the force balance, the hydrophopic force, whose origin is currently poorly understood.[36] However, for high T the force balance is (due to the hydrophobic force) shifted again toward the attractive force, and the polyelectrolyte starts to collapse.

These considerations show that an increase in T or I changes the conformation of polyelectrolytes from a stretched to a collapsed state due to the reduced dominance of the electrostatic forces in the force balance. Interestingly, the same trend is found for the size of the polyelectrolyte complexes in Figure 9: i.e., rather small complexes for low I and T and an increase in complex size for rising I and T.

Hence, we conclude that the size of the complexes is an indicator for the balance between attractive and repulsive forces acting on the monomers in solution. Small complexes can be attributed to the dominance of electrostatic forces for low I and T, which leads (due to the strong electrostatic attraction between oppositely charged polyelectrolyte and PEM) to rather flat and stratified polyelectrolyte layers. Furthermore, an increase in I and T also weakens the electrostatic attraction, which changes the polyelectrolyte conformation into a more coiled state and leads to thicker and less stratified layers.

However, this is a microscopic view on the (conformational) properties of single polyelectrolyte chains, whereas the complex growth indicates that a rise in I and T increases the number of PAH and PSS chains, which aggregate into one complex. This is a process involving several polyelectrolyte chains, and hence, the interpretation has to be generalized.

This can be easily done by understanding the complex growth not in terms of a force balance but in terms of the solvent quality: If the electrostatic force dominates the force balance, a stretched conformation of the chain is found and (compared to the Gaussian coil) the polyelectrolyte appears swollen. Hence, under these conditions (low I and T) the aqueous solution appears as a good solvent for

the polyelectrolyte, and precipitation is unlikely (due to the electrostatic chain−chain repulsion). A contraction of the polyelectrolyte chains can be induced by an increase in I or T, which may lead to a complete chain collapse at high salt concentration or high temperature. As under these conditions the attractive forces govern over the electrostatic interaction, the net chain−chain attraction leads to precipitation of the polyelectrolyte out of solution (e.g., salting out of polyelectrolytes[37]), and the solution becomes a bad solvent for the polyelectrolytes. Hence, with decreasing solvent quality the polyelectrolytes try to escape from solution and collect at the PEM−solvent interface. The increased surface coverage due to decrease of solvent quality is well-known for neutral polymers.[30] Here, it promotes the growth of the PE complexes within the PEM.

Therefore, the growth in complex size can be understood by a decrease in solvent quality by increasing I or T. Furthermore, using Figure 9, we are able to not only estimate the magnitude of the electrostatic force (with respect to the remaining nonelectrostatic forces) but also estimate the solvent quality for given values of I and T.

Please note that these considerations include temperature-induced precipitation of the polyelectrolytes only for T exceeding a critical value (i.e., T_{crit}). However, one often finds that the polyelectrolyte can be dissolved only if T is in between an upper and lower critical solution temperature (UCST and LCST, respectively[30]), i.e., for UCST $< T <$ LCST. (Please note that in contrast to the denomination UCST is usually a lower temperature than LCST, i.e., UCST < LCST.)

Hence, the precipitation of PSS due to the dominance of hydrophobic forces (i.e., for temperatures exceeding 55 °C at I = 1 M NaCl[38]) can be interpreted as a LCST-type critical temperature. Furthermore, Hirose et al. report[39] on theta conditions for PSS for T_{theta} = 16.8 °C and I = 4.17 M NaCl, and additionally, Serhalti et al.[40] were able to show that PSS undergoes a coil-to-globule transition if the temperature is decreased from 18 to 10 °C at I = 4.17 M NaCl. Hence, we conclude that PSS has an UCST-type critical temperature around 15 °C at I = 4.17 M NaCl.

The precipitation of PSS for $T <$ UCST can be understood using the Flory−Huggins theory,[30] which shows that under these conditions the gain in mixing entropy is to small to compensate the change in free enthalpy upon mixing of polymer and solvent. Hence, solvation of the polymer increases Gibbs free energy, which is thermodynamically not favorable.

However, a decrease of I leads to an increase in electrostatic monomer−monomer repulsion and opposes the chain collapse. Hence, for PSS this UCST can only be found at high I, and we conclude that a decrease in I shifts UCST to lower temperatures (which are not accessible in our experiments).

To summarize, these considerations show that the solvent quality is reduced if the temperature is changed toward UCST or LCST and that for $T <$ UCST or $T >$ LCST the solution behaves like a bad solvent. Furthermore, an increase in I leads also to a worsening of the solvent quality. Both effects can superimpose each other; i.e., often one observes that an increase in I rises UCST and decreases LCST,[41,42] which leads to a narrowing of the solubility temperature interval UCST $< T <$ LCST.

The discussion shows further that the solvent quality can be estimated from the complex size: a large and constant complex size (with respect to changes in I or T) indicates that the influence of the electrostatic force on the force balance can be neglected, and hence, we expect a worsening of the solvent quality under these conditions.

This idea is used in Figure 9 for drawing the dashed line, which separates the values of I and T expected to give good solvent conditions (I and T below the dashed line) from the values expected to worsen the solvent quality (I and T above the dashed line). Furthermore, the shaded areas in Figure 9 give the preparation conditions, which lead to a destabilization of the PEM due to spinodal decomposition. Interestingly, spinodal decomposition occurs always at values of I and T, which are associated with a worsening of solvent quality.

Influence of Salt Concentration and Temperature on the Deposition Mechanism during PEM Formation. Taking these facts together, we conclude that there are (at least) two different deposition mechanisms during the formation of PEM. At low I and T (white area below the dashed line in Figure 9) the electrostatic interaction dominates the system, leading to a strong electrostatic attraction between the oppositely charged polyelectrolytes and the formation of many electrostatically bound monomer pairs. This strong attraction leads to a rather regular deposition of polyelectrolyte layers and hence to stable PEMs.

However, an increase in I and T reduces the influence of the electrostatic interaction and worsens the solvent quality as the force balance (in solution) is shifted from repulsive toward attractive forces (e.g., of hydrophobic or entropic origin). Hence, under these conditions (shaded area in Figure 9) the deposition of the polyelectrolyte layers seems to be governed by nonelectrostatic interactions. This strongly reduces the stability of the PEMs, which now show spinodal decomposition.

Furthermore, the different precipitation mechanisms by approaching the UCST or LCST are also visible in the data. As already mentioned the LCST of PSS and PAH is often attributed to a strong increase of the hydrophobic force, which is a force of large magnitude and which would explain the large increase in bilayer thickness (cf. Figure 2a) for temperatures going toward LCST.

On the other hand, the UCST of these polyelectrolytes is often explained using Flory−Huggins theory.[30] The "additional" attractive force (arising by approaching the UCST) seems to be much weaker with respect to the hydrophobic force, as the UCST for PSS is observed only at very high salt concentrations (where electrostatic repulsion can be completely neglected). Hence, we conclude that this force is to weak to induce a noticeable increase in bilayer thickness (cf. Figure 2a). This provides further arguments why a decrease in solvent quality leads only at high temperatures (for T in the vicinity of LCST) to an increase in bilayer thickness.

Initiation of the Decomposition. To close our investigations, we address the question of when the decomposition of the film starts. Therefor, we prepared a 5.5-bilayer sample at I = 2 M NaCl and T = 45 °C and investigated the surface morphology with AFM in solution directly after deposition of the multilayer. Interestingly, the multilayer has completely different morphologies in solution (cf. Figure 10a) and after drying (cf. Figure 10c). In solution, neither the coarse structure (indicative of spinodal decomposition) nor the fine structure from Figure 8 is visible. Furthermore, the multilayer seems to be covered by small polyelectrolyte aggregates (height ~10 nm, lateral separation approximately 60 nm > 30 nm of the fine structure), which are mostly homogeneously distributed over the surface. However, this layer exhibits small hills that have the same surface structure than the rest of the layer (cf. amplitude image in Figure 10b).

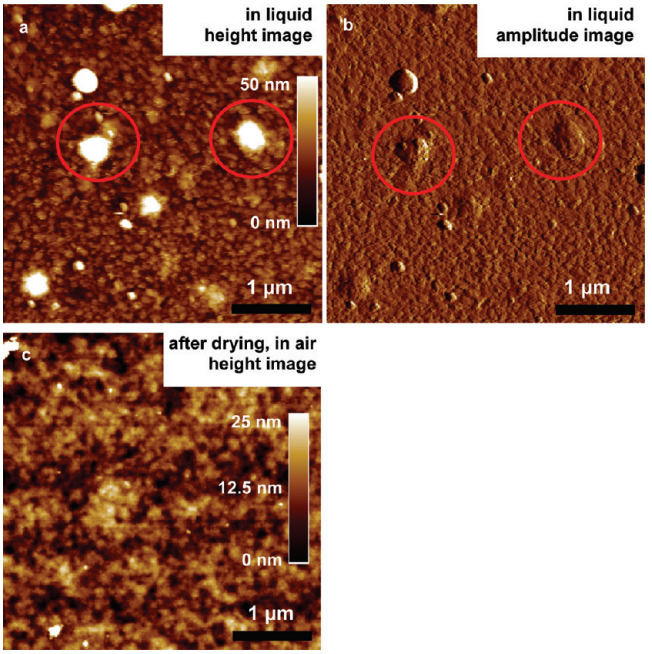

Figure 10. Surface morphology of a 5.5-bilayer PEM prepared at T = 45 °C and I = 2 M NaCl. In (a, b) the morphology was measured in deionized water directly after deposition of the last PE layer, whereas (c) shows the morphology in air after drying of the PEM film. Obviously, the PEM film exhibits a completely different structure after deposition and after drying; the latter shows evidence for the onset of spinodal decomposition. Furthermore, the PEM film appears to be slightly instable even in solution: in (a, b) two elevations are marked by circles, and interestingly, these elevations show the same surface structure (cf. deflection in (b)) as the rest of the film. Hence, we conclude that these elevations are parts of the PEM film, slightly detached from the substrate.

We interpret these hills as parts of the multilayer, which are not as tightly bound to the preceding bilayers as the rest of the film and which buckle. Furthermore, we take this as hint that the layer might be slightly mechanically instable. After drying (cf. Figure 10c), the multilayer appears as in previous measurements (cf. Figure 4d) and shows marks of a decomposition process. However, in this case the decomposition led to corrugations, which are much smaller compared to Figure 4d, which is presumably due to the changed drying routine.

Therefore, we conclude that the decomposition process starts with the drying of the multilayer, which increases the polyelectrolyte concentration within the multilayer (with respect to water) and drives the composition of the PEM−water mixture into the unstable (spinodal) region of the phase diagram.

Interestingly, high deposition temperatures seem to promote the kinetics of the decomposition process. Figure 4 shows, on the one hand, that the corrugations (caused by spinodal decomposition) increase with increasing deposition temperature. On the other hand, from Figure 10c one can infer that progress in decomposition is slowed down, if the multilayer is deposited at a certain temperature and afterward cooled to room temperature before drying. At the moment, we are not able to distinguish whether the kinetics are only slowed down or completely frozen at room temperature.

We conclude that the observed surface morphology for adsorption under bad solvent conditions cannot be explained by osmotic shocks (acting upon the PEM), which are expected to occur during washing performed in salt free (Milli-Q) water (compared to the high ionic strength adsorption solutions). If osmotic shocks would be responsible for such-like rearrangements, then they should be visible also in the wet state of the PEM. However, Figure 10a shows that this is obviously not the case and that the trigger of decomposition is found rather in drying than in washing the PEM. Hence, washing the PEM in solutions of high ionic strength is not expected to increase the stability of the deposited film.

Conclusion

Polyelectrolyte multilayers from PAH and PSS are formed from NaCl solutions at different temperatures. Both salt concentration (0.15−4 M NaCl) and temperature (5−55 °C) of the preparation solution are varied systematically. At a salt concentration of 0.15 M NaCl, the influence of the temperature is very weak, yet for 1 mol/L it is pronounced. It is found that below a critical temperature T_{crit} the thickness of a polycation/polyanion pair d_{BL} is constant and is only influenced by the ionic strength as published previously.[15] For T_{crit}, a nonmonotonic ionic strength dependence with a minimum at 3 M NaCl is observed (40 °C at 1 M, 30 °C at 2 M, 15 °C at 3 M, and 25 °C at 4 M NaCl). Interestingly, for deposition temperatures below T_{crit}, the surface roughness of the PEMs is small and approximately constant (10−15 Å for I = 0.15−3 M NaCl) or increases when the preparation temperature is cooled (4 M NaCl).

Apparently, the preparation conditions below the critical temperature T_{crit} and above the UCST (e.g., 16.7 °C for 4.17 M NaCl for PSS[39,40]) are a regime of good solvent quality. Electrostatic interactions dominate the adsorption of the polyelectrolytes. On drying, the polyelectrolyte tails and loops (which dangle into the solution) have to rearrange and collapse onto the PEM. Apparently, this process is strongly influenced by the ionic strength and affects the size of the dried polyelectrolyte complexes, which can be observed as fine structure with AFM (size 12−22 nm) and which gives the constant surface roughness of 10−15 Å. Any chain rearrangement on drying occurs on the nanometer scale. Furthermore, these multilayer films are stable, and it is possible to obtain a high amount of deposition steps without noticeable increase in layer roughness.

However, a worsening of the solvent quality (e.g., by an increase of the salt concentrations and for temperatures beyond the respective critical solution temperatures) reduces the influence of the electrostatic interaction further, and the multilayer formation is governed by nonelectrostatic interactions. This leads in the case of hydrophobic attraction acting between the PEM and the adsorbing molecules to a large increase in bilayer thickness (observed when approaching the LCST, i.e., by heating the preparation solution). In other words, more polyelectrolyte is deposited during one adsorption step. Yet bad solvent quality does not necessarily mean increased attraction between the PEM and the adsorbing polyelectrolyte. This is observed when approaching the UCST for very high salt concentrations, where we find no noticeable effect on the bilayer thickness.

However, PEMs prepared in the bad solvent regime are instable and show spinodal decomposition on drying, which leads to a pronounced increase in PEM roughness. The grain size is finite (about 22−30 nm) and independent of the deposition conditions. Note that the grain size under water (cf. Figure 10) is about 50−60 nm, suggesting a rearrangement on the molecular scale.

Nevertheless, the process of spinodal decomposition belongs to a general class of phenomena in which noise—whether equilibrium thermal noise or random variations originating from the history of the sample—is amplified. Because the amplification mechanism is wavelength selective (even though the initial noise is present at a very wide range of length scales), the final pattern,

while random, is characterized by a single length, a feature which we observe.[43−45] The length scale depends on the preparation conditions and is big; it always exceeds 100 nm. It is suggested that the decomposition occurs during film drying since the film morphology in water shows no decomposition pattern, even when the solution is cooled. As the PEM is much more instable and detachment of adsorbed layers might occur, it is difficult to obtain a high bilayer count in this regime.

Concluding, both growing regimes (good and bad solvent quality) appear to have different forces governing the layer buildup.

Acknowledgment. This work was supported by the Stiftung Alfried Krupp Kolleg Greifswald and the BMBF (FKZ 03Z2CKI with the ZIK HIKE project) as well as the state of Mecklenburg-Vorpommern. We thank Ralf Seemann for helpful discussions and referee 1 for thought-provoking suggestions.

Supporting Information Available: X-ray reflectivity data and the fits to a one-slab model for PEMs prepared at $I = 0.15$, 1, 3, and 4 M NaCl; furthermore, one figure showing a histogram of the average distance of the polyelectrolyte complexes (forming the fine structure) to their six next neighbors (preparation conditions: $I = 0.15$ M NaCl, $T = 15$ °C); surface morphologies of PEMs prepared at $I = 0.15$, 1, and 3 M NaCl. This material is available free of charge via the Internet at http://pubs.acs.org.

References and Notes

(1) Ahrens, H.; Förster, S.; Helm, C. A. *Phys. Rev. Lett.* **1998**, *81*, 4172.
(2) Li, F.; Balastre, M.; Schorr, P.; Argillier, J.-F.; Yang, J.; Mays, J. W.; Tirrell, M. *Langmuir* **2006**, *22*, 4084–4091.
(3) Decher, G. *Science* **1997**, *277*, 1232.
(4) Caruso, F.; Caruso, R. A.; Möhwald, H. *Science* **1998**, *282*, 1111.
(5) Yoo, P. J.; Nam, K. T.; Qi, J. F.; Lee, S. K.; Park, J.; Belcher, A. M.; Hammond, P. T. *Nat. Mater.* **2006**, *5*, 234.
(6) Dubois, M.; Schönhoff, M.; Meister, A.; Belloni, L.; Zemb, T.; Möhwald, H. *Phys. Rev. E* **2006**, *74*, 051402.
(7) Hiller, J.; Mendelsohn, J. D.; Rubner, M. F. *Nat. Mater.* **2002**, *1*, 59.
(8) Decher, G.; Hong, J. D.; Schmitt, J. *Thin Solid Films* **1992**, *210*, 831–835.
(9) Decher, G.; Schmitt, J. *Prog. Colloid Polym. Sci.* **1992**, *89*, 160–164.
(10) Netz, R. R.; Joanny, J. F. *Macromolecules* **1999**, *32*, 9026.
(11) Netz, R. R.; Andelman, D. *Phys. Rep.* **2003**, *380*, 1–95.
(12) Schmitt, J. Thesis, Johannes Gutenberg-Universität: Mainz, **1996**.
(13) Cosgrove, T.; Obey, T. M.; Vincent, B. *J. Colloid Interface Sci.* **1986**, *111*, 409–418.
(14) Ahrens, H.; Baltes, H.; Schmitt, J.; Möhwald, H.; Helm, C. A. *Macromolecules* **2001**, *34*, 4504–4512.
(15) Lösche, M.; Schmitt, J.; Decher, G.; Bouwman, W. G.; Kjaer, K. *Macromolecules* **1998**, *31*, 8893–8906.
(16) Tan, H. L.; McMurdo, M. J.; Pan, G.; Van Patten, P. G. *Langmuir* **2003**, *19*, 9311–9314.
(17) Büscher, K.; Graf, K.; Ahrens, H.; Helm, C. A. *Langmuir* **2002**, *18*, 3585–3591.
(18) Salomäki, M.; Vinokurov, I. A.; Kankare, J. *Langmuir* **2005**, *21*, 11232–11240.
(19) Gopinadhan, M.; Ivanova, O.; Ahrens, H.; Günther, J.-U.; Steitz, R.; Helm, C. A. *J. Phys. Chem. B* **2007**, *111*, 8426–8434.
(20) Gao, C.; Leporatti, S.; Donath, E.; Möhwald, H. *J. Phys. Chem. B* **2000**, *104*, 7144–7149.
(21) Leporatti, S.; Voigt, A.; Mitlöhner, R.; Sukhorukov, G.; Donath, E.; Möhwald, H. *Langmuir* **2000**, *16*, 4059–4063.
(22) Helm, C. A.; Möhwald, H.; Kjaer, K.; Als-Nielsen, J. *Europhys. Lett.* **1987**, *4*, 697–703.
(23) Parratt, L. G. *Phys. Rev.* **1954**, *95*, 359–369.
(24) Asmussen, A.; Riegler, H. *J. Chem. Phys.* **1996**, *104*, 8159–8164.
(25) Straňák, V.; Čada, M.; Quaas, M.; Block, S.; Bogdanowicz, R.; Kment, Š.; Wulff, H.; Hubička, Z.; Helm, C. A.; Tichý, M.; Hippler, R. *J. Phys. D* **2009**, *42*, 105204.
(26) Hesselink, F.Th. *J. Colloid Interface Sci.* **1977**, *60*, 448.
(27) Yim, H.; Kent, M.; Matheson, A.; Ivkov, R.; Satija, S.; Majewski, J.; Smith, G. S. *Macromolecules* **2000**, *33*, 6126–6133.
(28) Steitz, R.; Leiner, V.; Siebrecht, R.; von Klitzing, R. *Colloids Surf., A* **2000**, *163*, 63–70.
(29) Böhmer, M. R.; Evers, O. A.; Scheutjens, J. M. H. M. *Macromolecules* **1990**, *23*, 2288–2301.
(30) Fleer, G. J.; Cohen Stuart, M. A.; Scheutjens, J. M. H. M.; Cosgrove, T.; Vincent, B. *Polymers at Interfaces*; Chapman & Hall: London, 1993.
(31) Israelachvili, J. N. *Intermolecular and Surface Forces*; Academic Press: London, 1991.
(32) Hillert, M. Sc.D. Thesis, Massachusetts Institute of Technology, Cambridge, MA, 1956.
(33) Sofonea, V.; Mecke, K. R. *Eur Phys. J. B* **1999**, *8*, 99–112.
(34) Cahn, J. W.; Hilliard, J. E. *J. Chem. Phys.* **1958**, *28*, 258–267.
(35) Galenko, P.; Lebedev, V. *Int. J. Thermodyn.* **2008**, *11*, 21–28.
(36) Meyer, E. E.; Rosenberg, K. J.; Israelachvili, J. *Proc. Natl. Acad. Sci. U.S.A.* **2006**, *103*, 15739–15746.
(37) Volk, N.; Vollmer, D.; Schmidt, M.; Oppermann, W.; Huber, K. *Adv. Polym. Sci.* **2004**, *166*, 29–66.
(38) Gopinadhan, M.; Ahrens, H.; Günther, J. U.; Steitz, R.; Helm, C. A. *Macromolecules* **2005**, *38*, 5228–5235.
(39) Hirose, E.; Iwamoto, Y.; Norisuye, T. *Macromolecules* **1999**, *32*, 8629–8634.
(40) Serhatli, E.; Serhatli, M.; Baysal, B. M.; Karasz, F. E. *Polymer* **2002**, *43*, 5439–5445.
(41) Liu, X.-M.; Wang, L.-S. L.-S.; Wang, L.; Huang, J.; He, C. *Biomaterials* **2004**, *25*, 5659–5666.
(42) Suwa, K.; Yamamoto, K.; Akashi, M.; Takano, K.; Tanaka, N.; Kunugi, S. *Colloid Polym. Sci.* **1998**, *276*, 529–533.
(43) Higgins, A. M.; Jones, R. A. L. *Nature* **2000**, *404*, 476–478.
(44) Seemann, R.; Herminghaus, S.; Jacobs, K. *Phys. Rev. Lett.* **2001**, *86*, 5534–5537.
(45) Seemann, R.; Herminghaus, S.; Jacobs, K. *J. Phys.: Condens. Matter* **2001**, *13*, 4925–4938.